

# Characterisation of commercial SiC MOSFETs at deep-cryogenic temperatures

Megan Powell,<sup>1</sup> Euan Parry,<sup>1</sup> Conor McGeough,<sup>1</sup> Alexander Zotov,<sup>1</sup> and Alessandro Rossi<sup>1,2,\*</sup>

<sup>1</sup>*Department of Physics, SUPA, University of Strathclyde, Glasgow G4 0NG, United Kingdom*

<sup>2</sup>*National Physical Laboratory, Hampton Road, Teddington TW11 0LW, United Kingdom*

Silicon carbide is a wide-bandgap semiconductor with an emerging CMOS technology platform and it is widely deployed in high power and harsh environment electronics. This material is also attracting interest for quantum technologies through its crystal defects, which can act as spin-based qubits or single-photon sources. In this work, we assess the cryogenic performance of commercial power MOSFETs to evaluate their suitability for CMOS-compatible quantum electronics. We perform a statistical study of threshold voltage and subthreshold swing from 300 K down to 650 mK, focusing on reproducibility and variability. Our results show significant performance degradation at low temperatures, including large gate hysteresis, threshold voltage shifts, and subthreshold swing deterioration. These effects suggest instability in electrostatic control, likely due to carrier freeze-out and high interface trap density, which may pose challenges for the reliable use of this transistor technology towards the realisation of quantum devices or cryo-CMOS electronics.

## I. INTRODUCTION

Silicon carbide (SiC) is a wide-bandgap semiconductor extensively deployed in commercial applications, such as high-power and harsh environment electronics [1, 2]. In contrast to other wide-bandgap materials, SiC is the only system that has demonstrated realistic prospects towards the realisation of analog and digital building blocks at integrated circuit level. This has been possible through the development of foundry-based 4H-SiC complementary metal-oxide-semiconductor (CMOS) technology [3, 4].

SiC has more recently also attracted attention in the field of quantum technologies [5]. Specifically, intrinsic or implanted defects in the SiC crystal can function as spin-based quantum bits (qubits) [6] or environmental sensors [7] and exhibit spin-dependent photonic emission, offering potential for both quantum computing and networking [8]. Current methods for addressing quantum states in SiC rely on optical scanning techniques on barely processed wafers, an approach not directly amenable to integration or mass production. Exploiting the existing SiC CMOS transistor technology towards quantum state control and readout could pave the way for industry-compatible integrated quantum electronics, an approach that is already gaining momentum in other CMOS-compatible materials [9], primarily in silicon [10].

A critical step in validating SiC MOS systems as a platform for integrated quantum technologies is the evaluation of their electronic properties at cryogenic temperatures. Low-temperature operation is often indispensable for preserving fragile quantum attributes against thermal fluctuations. For example, spin state readout systems based on electrometry [11], must be operated at 4 K or below to achieve good sensitivity via charge quantisation. Understanding SiC MOSFETs behaviour at such temperatures may therefore be important for envisaging analo-

gous electrical readout schemes [12] or designing cryo-CMOS control electronics [13, 14]. To this aim, some desirable features should be high-quality ohmic contacts for ease of control of the charge reservoirs, sharp channel gating and/or pinch-off to fine tune confinement potentials, as well as overall reproducibility and stability of transport characteristics.

In this work, we characterise SiC power MOSFETs at cryogenic temperatures with an eye to ascertain whether current commercial devices and processes already hold prospect for the realisation of integrated quantum electronics. We carry out a statistical study of threshold voltage and subthreshold swing, considered to be key metrics to assess reproducibility and stability. We study two nominally identical commercial transistors in a wide temperature range from 300 K down to 650 mK and report similar cryogenic behavior. In general, we observe a systematic degradation of device performance, as the temperature of operation is decreased. We suggest that a combination of carrier freeze-out and high trap density are responsible for increased levels of gate voltage hysteresis, long-term drift and charge instability.

## II. METHODS

The devices under test are two nominally identical bare die n-channel 1.2 kV 4H-SiC MOSFETs developed by Wolfspeed (CPM3-1200-0013A). For convenience, they will be named *Device A* and *Device B*. These devices are vertical diffusion MOSFETs with source (S) and gate (G) metal contacts located at the top of the chip, whilst the drain (D) contact occupies the entire flip side of the chip. Due to often analogous results between the two samples, on occasions only one device's analysis is presented in the main text (see appendix for comprehensive datasets).

We measure transport characteristics at multiple temperatures by thermal anchoring the sample holder containing each bond-wired chip onto the mixing chamber plate of a dilution refrigerator. The plate temperature ( $T$ ) can be controlled with dedicated heating devices and

\* Email: alessandro.rossi@strath.ac.uk

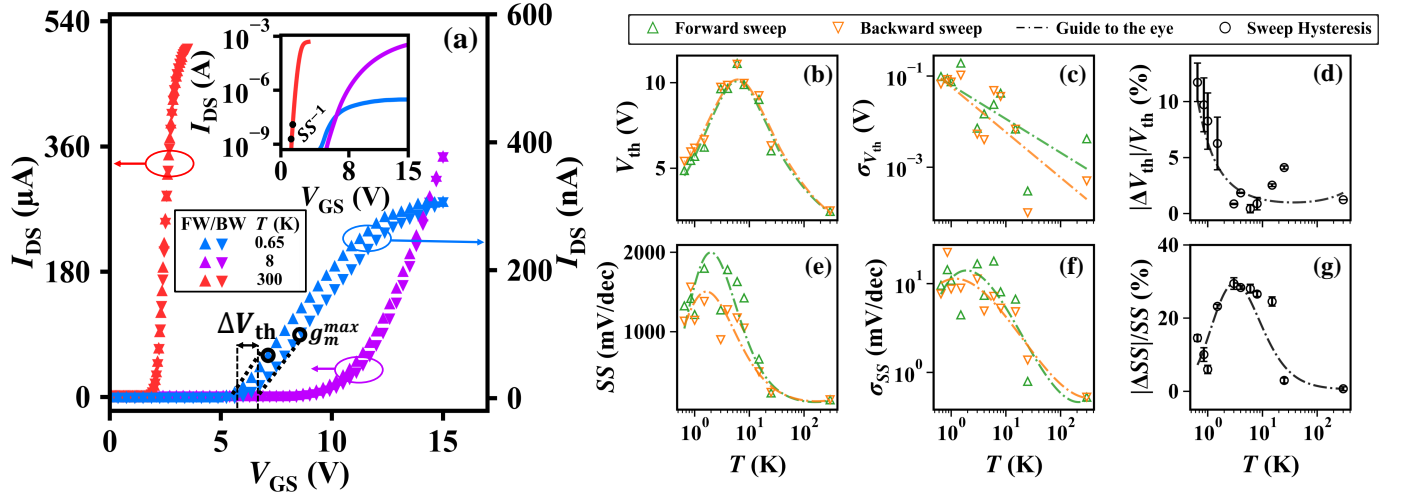


FIG. 1. Device A characteristics and parameters as a function of temperature. (a) Measured  $I_{DS}$ - $V_{GS}$  transfer characteristics at  $T = 0.65$  K, 8 K, 300 K (blue, purple and red triangles, respectively).  $V_{DS}^{0.65\text{ K}} = 3.8$  V,  $V_{DS}^{8\text{ K}} = 2.4$  V and  $V_{DS}^{300\text{ K}} = 0.05$  V. FW (upper pointed triangles) and BW (downward pointed triangles) indicate the forward (increasing) and backward (decreasing) voltage sweep direction, respectively. The black circles on the  $T = 0.65$  K dataset indicate the points of maximum transconductance used to extract  $V_{th}$  from linear fits, the associated  $\Delta V_{th}$  due to hysteresis is also shown. The insert displays the same forward sweep data as in the main panel on a semi-log scale. The current values at which SS is calculated are indicated by black dots. Parameters extracted from statistical distributions of 50 characteristics as functions of temperature: (b)  $V_{th}$ , (c)  $\sigma_{V_{th}}$ , (d)  $|\Delta V_{th}|/V_{th}$ , (e)  $SS$ , (f)  $\sigma_{SS}$ , (g)  $|\Delta SS|/SS$ . The dot-dashed lines in each panel represent guides to the eye to aid evaluation of temperature dependencies. The error bars in (d) and (g) indicate a  $\pm 1\sigma$  spread of the relevant distribution.

we set  $0.65\text{ K} \leq T \leq 25\text{ K}$ . Even though the refrigerator is capable of reaching temperatures as low as tens of millikelvin, the device power dissipation during operation generates sufficient heat to exceed the cooling power of the cryogenic system. This has prevented us from achieving a stable temperature for measurements below approximately 0.65 K, which has been therefore set as our lower experimental temperature bound.

Two separate source-measure units (SMU) are employed for acquiring IV traces. One SMU is used across drain-source contacts to apply bias voltage ( $V_{DS}$ ), and measure current ( $I_{DS}$ ). The other SMU is used to apply gate voltage ( $V_{GS}$ ), whilst monitoring that the leakage current ( $I_{GS}$ ) remains within nominal values of operation set by the manufacturer, i.e.  $I_{GS} \leq 30$  nA. The source contact is always kept at reference ground defined by the Low terminal of an SMU. All output and transfer characteristics are acquired in Kelvin mode to minimise voltage drop contributions from the set-up wiring. To robustly investigate each performance metric, we have built statistically relevant datasets by acquiring the same IV trace at least 50 times per temperature (see appendix). This has enabled us to record not only the temperature dependence of each parameter of interest, but also how their repeatability and stability were affected by temperature and voltage sweep direction.

### III. RESULTS

#### A. Device Performance

Figure 1(a) shows  $I_{DS}$ - $V_{GS}$  transfer characteristics at three representative temperatures (see additional traces in appendix). From these characteristics, we extract two parameters, i.e. the device's threshold voltage ( $V_{th}$ ) and the subthreshold swing ( $SS$ ). The former is obtained as the zero current intercept by a linear extrapolation from the point of maximum transconductance ( $g_m^{max}$ ) [15], as shown in the main panel. Note that each transfer characteristics is measured at a different  $V_{DS}$ , depending on the temperature of operation. This stems from the fact that S/D contacts develop an increasingly severe Schottky-type behavior as temperature decreases and, therefore, we need to increase  $V_{DS}$  accordingly to attain transport through the transistors. To account for the effect of different bias on the extracted  $V_{th}(T)$ , we quote all threshold voltages at an equivalent  $V_{DS} = 2$  V, by using an extrapolation technique discussed in Section III B.

$SS$  is obtained by calculating the inverse gradient of the log-linear characteristics in the weak inversion regime achieved at two fixed values of current ( $I_{DS,1} = 2$  nA;  $I_{DS,2} = 10$  nA):

$$SS = \frac{dV_{GS}}{dI_{DS}} = \frac{V_{GS}(I_{DS,2}) - V_{GS}(I_{DS,1})}{\log_{10}(I_{DS,2}) - \log_{10}(I_{DS,1})} \quad (1)$$

as illustrated in the insert.

The results of the statistical study of device parameters as functions of temperature are shown in Fig. 1(b)-(g). Figure 1(b) illustrates the dependence of  $V_{th}$  on temperature. One can see that with decreasing temperature from ambient conditions, it increases to a maximum value of  $V_{th} \approx 11$  V achieved at  $T \approx 8$  K and then steadily drops at deeper cryogenic temperatures. At the higher end of the temperature range, there is a very good agreement between data measured by increasing (forward mode, FW) and decreasing (backward mode, BW)  $V_{GS}$ . This agreement progressively deteriorates as the temperature decreases, particularly to the left of the voltage peak ( $T \leq 8$  K). We suggest that the non-monotonic behavior of  $V_{th}(T)$  can be ascribed to competing temperature effects in intrinsic carrier concentration, acceptor freeze-out and interface trap occupancy. In particular, it has been observed before in similar devices that  $V_{th}$  increases with decreasing temperature because interface traps become increasingly negatively charged and intrinsic carrier density reduces [16, 17]. It is plausible that these two effects saturate for sufficiently low temperature, say around 8 K in our case. For lower  $T$ , freeze-out in the p-type channel region may result in a sharp decrease in the Fermi surface potential and, consequently, in the threshold voltage. The temperature at which the crossover between different dominant effects occurs is likely dependent on device doping profile and density of interface traps. In fact, for other SiC MOSFET technologies this has been observed at higher temperatures [18].

Figure 1(c) illustrates the statistical spread of  $V_{th}(T)$  ( $\sigma_{V_{th}}$ ), as obtained from the standard deviation of a Gaussian fit to the histogram built with 50 nominally identical IV runs (see appendix). One can see an overall increase of distribution spread for decreasing temperature, which indicates that the devices are subject to increasing instabilities at cryogenic conditions. Interestingly, at the highest temperatures, the instabilities appear to be more marked for the FW measurement mode, whereas at the lowest end of the range the distinction between FW and BW mode tends to fade away. In Fig. 1(d), we measure the effect of gate voltage hysteresis on  $V_{th}(T)$ . Specifically, we calculate  $\Delta V_{th} = V_{th}^{BW} - V_{th}^{FW}$  at each temperature of interest. The plot shows that the relative shift in threshold is quite small (few percent) and approximately constant from room temperature down to  $T \approx 1.5$  K. At deeper cryogenic temperatures, a steady increase in hysteretic effects is observed. This is also accompanied by a stark increase in statistical spread (see error bars). We speculate that threshold voltage hysteresis and instability go hand in hand and may both originate from the large shift introduced by increasingly negatively charged interface traps [16].

In Fig. 1(e)-(g), a statistical analysis is reported for  $SS$ . Contrary to theoretical predictions for MOSFETs by which  $SS$  should steadily decrease with decreasing temperature [19], we see a significant growth down to approximately 4 K followed by a decrease at lower tem-

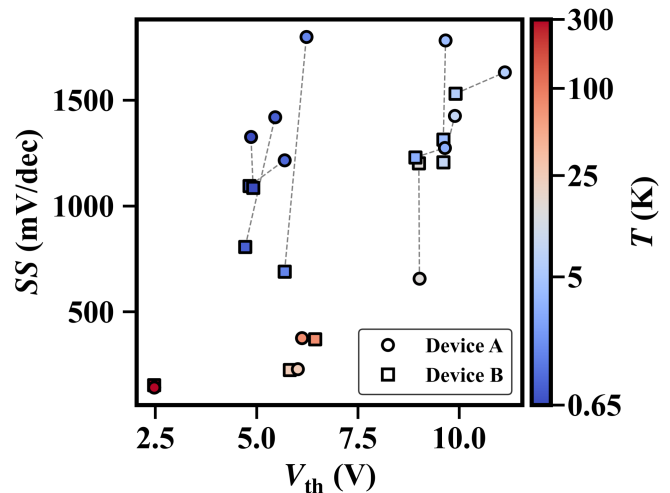


FIG. 2. Comparison of performance metrics ( $SS$ ,  $V_{th}$ ) between Device A (circles) and Device B (squares) as a function of temperature (color scale). Dashed lines are guides to the eye highlighting inter-device deviation at equal temperatures.

peratures, as indicated in panel (e). This is accompanied by a similar trend in statistical spread shown in panel (f). By calculating  $\Delta SS = SS^{FW} - SS^{BW}$ , one can conclude that the relative hysteresis is small at room temperature, but it peaks at about 30% at 4 K and substantially decreases at lower temperatures, as reported in Fig. 1(g). The rapid increase in  $SS$  with decreasing temperature is once again consistent with an increase in the density of SiC/SiO<sub>2</sub> interface traps [20], which ultimately degrades the transport characteristics. However, it appears that the performance slightly improves at deep cryogenic temperatures even though the room temperature situation is not fully restored at the lowest temperature of our experiments (0.65 K).

In Fig. 2, a comparison between the performance of Device A and B is presented as a function of temperature. One can notice that in the upper temperature range (roughly  $15 \text{ K} < T < 300 \text{ K}$ ) the agreement between device metrics is quite good, indicated by a modest separation between isothermal data points (dashed lines). However, as the temperature is further decreased this separation markedly increases. This is generally consistent with the observed degradation of device stability, which is likely contributing towards a more severe inter-device variability at deep cryogenic temperature.

## B. Cryogenic Schottky Contacts

As mentioned earlier, we observe increasingly non-linear S/D contact characteristics as temperature decreases. Figure 3(a) reports the normalised  $I_{DS}$  as a function of  $V_{DS}$  at three representative cryogenic temperatures. One can see a typical non-linear Schottky diode dependence with increasing turn-on voltages for

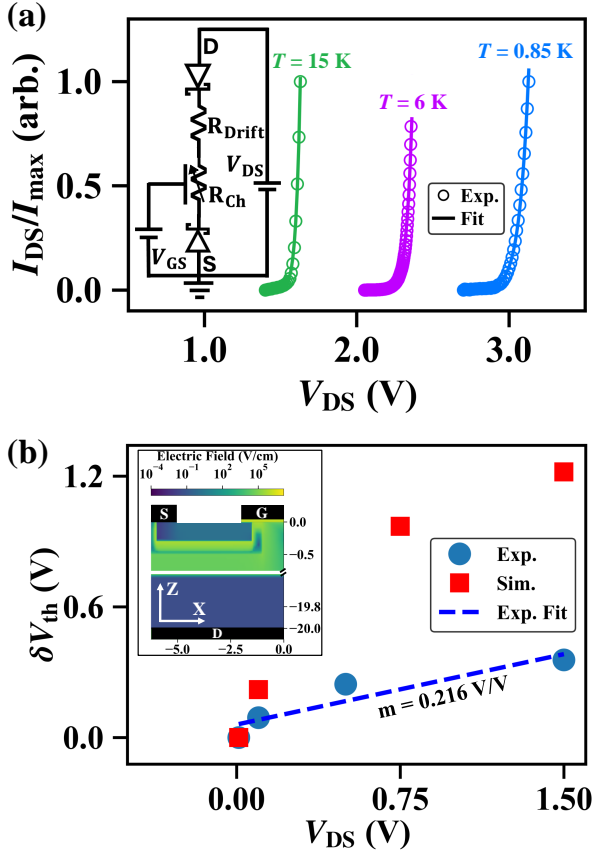


FIG. 3. (a) Device A normalised  $I_{DS}$ - $V_{DS}$  experimental curves and fits at  $T = 15$  K (green),  $T = 6$  K (purple) and  $T = 0.85$  K (blue).  $V_{GS}^{0.85\text{ K}} = 8$  V,  $V_{GS}^{6\text{ K}} = 10$  V and  $V_{GS}^{15\text{ K}} = 8$  V are chosen to be greater than  $V_{th}$  at the relevant temperature, so that the transistor is in the ON state. Insert depicts an equivalent circuit diagram of the device presenting the S/D contacts as Schottky diodes at cryogenic temperatures. (b)  $V_{th}$  shift as a function of  $V_{DS}$  from experiments (circles) and TCAD simulations (squares) at  $T = 300$  K. The dashed line indicates a linear fit to the experimental data used to obtain the correction factor employed to extrapolate  $V_{th}(T)$  at an equivalent  $V_{DS} = 2$  V for all temperatures (as reported in Fig. 1). The insert shows a representative electric field map in a vertical transistor of similar dimensions as the one measured, as obtained from TCAD simulations. The axis labels are in  $\mu m$ . Simulation is carried out at  $V_{DS} = 1.5$  V,  $V_{GS} = 10$  V.

decreasing temperature. Note that at room temperature the linear IV relationship expected for ohmic contacts is observed (not shown). We argue that, as temperature is reduced, carrier freeze-out in the  $n++$  contact regions makes tunneling through the metal-semiconductor Schottky barrier increasingly unfavorable due to an increase in barrier width ( $d$ ) [21]. Hence, the source and drain contacts, acting as Schottky diodes at cryogenic temperature, give rise to the equivalent circuit diagram shown in the inset of Fig. 3(a). The main circuit elements are a small channel resistance ( $R_{Ch}$ ) achieved by choosing  $V_{GS} \gg V_{th}$ , a freeze-out dependent resistance

of the transistor's drift region ( $R_{Drift}$ ) and two back-to-back Schottky diodes one for each of S and D contacts. We consider that the dominant component limiting the current is the S diode which operates in reverse bias mode, i.e. until this achieves reverse tunneling breakdown, only a limited current flows through the transistor. We model this scenario by assuming that thermionic emission is suppressed and fit the data using a Fowler-Nordheim tunneling model [15]:

$$I(V_{DS}) = A \frac{\alpha}{\phi} \left[ \frac{V_{DS} - V_0}{d} \right]^2 \exp \left( -\beta \frac{d\phi^{3/2}}{V_{DS} - V_0} \right) \quad (2)$$

where  $\alpha$  and  $\beta$  are fixed terms that can be calculated directly from constants of nature and the effective electron mass,  $A = 60 \text{ nm}^2$  is the estimated contact size of the S metal pad,  $\phi$  is the Schottky barrier height, which we keep constant ( $\phi = 0.9$  eV) because only mildly temperature dependent compared to other parameters. There are two fitting parameters:  $d$  and  $V_0$  (the voltage drop across temperature dependent  $R_{Drift}$ ). From the fits of several cryogenic IV curves, we see that both  $d$  and  $V_0$  increase with decreasing temperatures (see table in appendix). This indicates that at lower temperatures the tunnel barrier becomes increasingly thick and the drift region becomes more resistive. These findings are qualitatively consistent with the possible effects of carrier freeze-out. In fact, one expects an inverse quadratic relationship between the barrier width and the effective carrier density in the semiconductor side of a metal-semiconductor junction and an exponential decay of ionization-activated carriers [15, 21].

The need for relatively large and variable  $V_{DS}$  values to achieve transport at low temperatures may affect our ability to consistently extract  $V_{th}(T)$ . In fact, we observe a clear shift in  $V_{th}$  ( $\delta V_{th}$ ) when  $V_{DS}$  is changed, as shown in Fig. 3(b). In planar MOSFETs this is typically attributed to drain-induced barrier lowering, a well-established consequence of short-channel effects [15]. However, in our case the application of positive drain voltage has the opposite effect, as it operates in competition with the gate voltage by making it harder to invert the channel, leading to a positive voltage gradient (see dashed line). We assume that this effect is to first approximation temperature independent because related to device electrostatics alone. Hence, we use the room temperature experimental gradient shown in Fig. 3(b) as a correction factor ( $m$ ) to quote all  $V_{th}(T)$  obtained from the statistical studies at an equivalent  $V_{DS} = 2$  V.

To explain this electrostatic effect, we argue that it stems from the vertical architecture of the transistor which results in large  $V_{DS}$  having a gating effect in competition with the top gate electrode. To corroborate this assumption, we run Sentaurus TCAD simulations and study the electric field profile in the vertical transistor channel as a function of  $V_{DS}$ , see insert of Fig. 3(b). Similar to the experimental case, the threshold voltages extracted from the simulations show a positive gradient,



suggesting that the electrostatic effect of the drain electrode can be assimilated to a back gate. We acknowledge that in Fig. 3(b) the agreement between experimental and simulated  $\delta V_{th}$  is not excellent probably because the device physical dimensions used for the simulations do not match the real transistor size, which is not fully disclosed by the manufacturer. Nonetheless, the evidence of a drain-induced gating effect is robust, originating from electrostatic considerations alone.

### C. Device Drift and Training

We now turn to discuss significant instability in the device characteristics, which rendered necessary the establishment of a device training protocol prior to collection of the statistical datasets discussed so far. In Fig. 4(a), we show a significant  $I_{DS}$  drift when the device is left idle at the  $g_m^{\max}$  operation point. For all three representative temperatures examined, we observe an initial rapid current drop followed by a slower leveling off. We argue that this behavior is consistent with the dynamics of oxide-trap charging often reported for SiC MOSFETs [22]. To model this effect, we fit the experimental data to a double exponential decay function and extract two time constants relevant to the initial fast current drop ( $\tau_1$ ) and the slower saturation ( $\tau_2$ ). As shown in the insert of Fig. 4(a), although the two constants differ by approximately an order of magnitude, both decrease with decreasing temperature. This suggests that both processes responsible for the drift are increasingly fast in reaching steady states of operation the lower the temperature. Our observations are qualitatively in line with two oxide-trap charging mechanisms, one occurring rapidly because located at the semiconductor-oxide interface, and another one happening more slowly because located deeper into the oxide layer [23]. Both processes can be accelerated by reducing random thermal fluctuations, which, in turn, makes the gate electrostatics more efficient in attracting and trapping electrons at the oxide.

As shown in Fig. 4(a), it would have taken an impractically long time to wait for the current to reach a saturation point before collecting statistics. Hence, we implemented a protocol to accelerate the processes of oxide trapping, which we refer to as device training (also known as gate-bias stressing). In Fig. 4(b), we plot the maximum value of current reached during a training run ( $I_{Sat}$ ) as a function of the number of consecutive runs performed at  $T = 0.65$  K. Each run lasts approximately 165 s and is defined as a forward gate sweep followed by a reverse gate sweep which take the transistor from the OFF state to the ON saturation state and back. It is evident that through the training procedure the transport characteristics undergoes an initial ramp-up stage followed by a leveling off of the maximum current value after a critical amount of time, which we call the cumulative training time ( $t_{tr}$ ). This time is observed to depend on  $V_{DS}$  and can be reduced by running the protocol at

higher voltages, as depicted in the inset of Fig. 4(b). We applied this training protocol prior to the acquisition of IV characteristics every time the experimental temperature was modified.

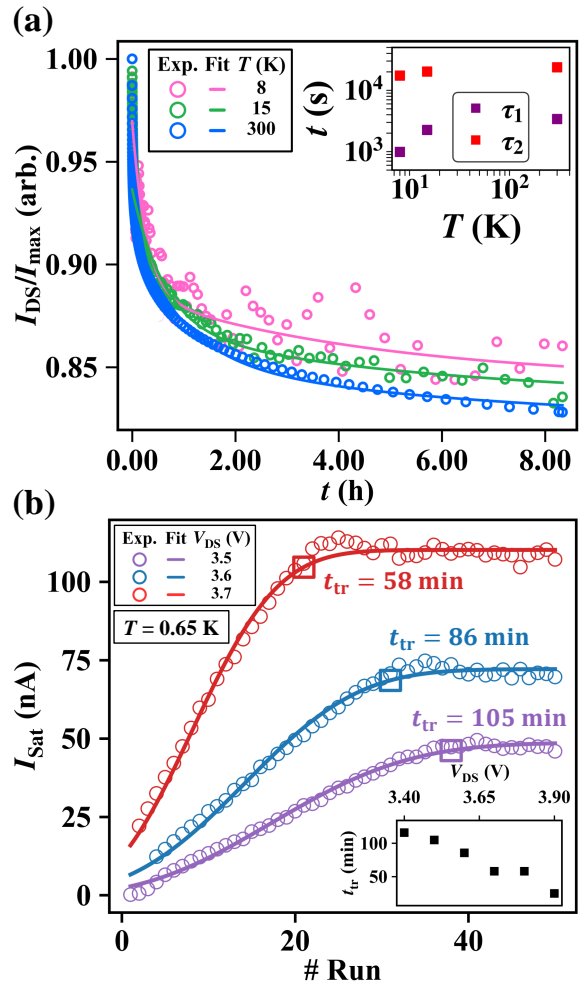


FIG. 4. (a) Device A's experimental  $I_{DS}$  drift (circles) and double exponential decay fits (solid lines) as a function of time at  $T = 8$  K (pink),  $T = 15$  K (green) and  $T = 300$  K (blue). The insert depicts the extracted time constants as a function of temperature. (b) Device B's training protocol at 0.65 K for  $V_{DS} = 3.5$  V (purple),  $V_{DS} = 3.6$  V (blue), and  $V_{DS} = 3.7$  V (red). Experimental  $I_{Sat}$  (circles) and fits (solid lines) as a function of runs. The fits are exponential functions with single time constants reaching 95% of the saturation current at the points indicated by squares. The insert depicts  $t_{tr}$  vs  $V_{DS}$  as extracted from the fits (squares in the main panel).

## IV. CONCLUSION

We have presented a statistical study of commercially available SiC power MOSFETs at deep cryogenic temperatures, to assess the viability of existing device technology for quantum applications. Our results suggest

that at present this is going to be unlikely (at least with the device technology examined here), as device performance, reliability and variability all deteriorate at low temperature. More specifically, the observation of significant voltage hysteresis, especially at deep cryogenic temperatures, indicates unstable and history-dependent electrostatic control. This behavior could severely limit the ability to form and tune quantum dots with repeatable and predictable charge occupancy, essential ingredients for both MOS readout electronics and qubit devices [12]. Furthermore, tunnel barriers in MOS quantum dots and electrometers are electrostatically defined by dedicated gate potentials shaping the conduction band edge [24]. A sharp potential barrier is typically required to control tunneling precisely. Our observation of a significant degradation of  $SS$  at cryogenic temperatures does not bode well for the use of SiC MOSFETs in this context, as it may indicate that the ability of modulating the channel potential is weak and negatively affected by interface traps or leakages. Lastly, the lack of high-quality ohmic contacts at low temperature is also adversely impacting the prospects of using these devices for quantum state readout. This stems from the need for fast readout electronics compatible with single-shot charge detection [11],

which would be difficult to implement with highly resistive contacts.

Despite these limitations, our findings also highlight specific technological targets that could make SiC a more viable platform for cryogenic quantum electronics. The main challenges we observe are primarily rooted in material science issues, such as interface trap density, oxide quality, and contact formation. Encouragingly, these are all areas where continued progress is being made within the SiC power device community. Beyond material-level improvements, further gains could be achieved through tailored device design choices, made possible by the increasingly mature CMOS technology available for SiC.

## ACKNOWLEDGMENTS

The authors thank V. Shah for useful discussions, as well as J. Gillan and A. Robbins for technical support. A.R. acknowledges support from the UKRI Future Leaders Fellowship Scheme (Grant agreement: MR/T041110/1).

- 
- [1] T. Kimoto, Material science and device physics in SiC technology for high-voltage power devices, *Japanese Journal of Applied Physics* **54**, 040103 (2015).
  - [2] P. French, G. Krijnen, and F. Roozeboom, Precision in harsh environments, *Microsystems & Nanoengineering* **2**, 16048 (2016).
  - [3] J. Romijn, S. Vollebregt, L. M. Middelburg, B. El Mansouri, H. W. van Zeijl, A. May, T. Erlbacher, G. Zhang, and P. M. Sarro, Integrated digital and analog circuit blocks in a scalable silicon carbide CMOS technology, *IEEE Transactions on Electron Devices* **69**, 4 (2021).
  - [4] J. Romijn, S. Vollebregt, L. M. Middelburg, B. El Mansouri, H. W. van Zeijl, A. May, T. Erlbacher, J. Leijtens, G. Zhang, and P. M. Sarro, Integrated 64 pixel UV image sensor and readout in a silicon carbide CMOS technology, *Microsystems & Nanoengineering* **8**, 114 (2022).
  - [5] D. D. Awschalom, R. Hanson, J. Wrachtrup, and B. B. Zhou, Quantum technologies with optically interfaced solid-state spins, *Nature Photonics* **12**, 516 (2018).
  - [6] N. T. Son, C. P. Anderson, A. Bourassa, K. C. Miao, C. Babin, M. Widmann, M. Niethammer, J. Ul Hassan, N. Morioka, I. G. Ivanov, F. Kaiser, J. Wrachtrup, and D. D. Awschalom, Developing silicon carbide for quantum spintronics, *Applied Physics Letters* **116**, 190501 (2020).
  - [7] J. B. S. Abraham, C. Gutzsell, D. Todorovski, S. Sperling, J. E. Epstein, B. S. Tien-Street, T. M. Sweeney, J. J. Wathen, E. A. Pogue, P. G. Brereton, T. M. McQueen, W. Frey, B. D. Clader, and R. Oslander, Nanotesla magnetometry with the silicon vacancy in silicon carbide, *Phys. Rev. Appl.* **15**, 064022 (2021).
  - [8] A. Lohrmann, B. C. Johnson, J. C. McCallum, and S. Castelletto, A review on single photon sources in silicon carbide, *Reports on Progress in Physics* **80**, 034502 (2017).
  - [9] N. Banerjee, C. Bell, C. Ciccarelli, T. Hesjedal, F. Johnson, H. Kurebayashi, T. A. Moore, C. Moutafis, H. L. Stern, I. J. Vera-Marun, J. Wade, C. Barton, M. R. Connolly, N. J. Curson, K. Fallon, A. J. Fisher, D. A. Gangloff, W. Griggs, E. Linfield, C. H. Marrows, A. Rossi, F. Schindler, J. Smith, T. Thomson, and O. Kazakova, *Materials for quantum technologies: a roadmap for spin and topology* (2024), [arXiv:2406.07720 \[cond-mat.mes-hall\]](https://arxiv.org/abs/2406.07720).
  - [10] M. F. Gonzalez-Zalba, S. de Franceschi, E. Charbon, T. Meunier, M. Vinet, and A. S. Dzurak, Scaling silicon-based quantum computing using CMOS technology, *Nature Electronics* **4**, 872 (2021).
  - [11] J. M. Elzerman, R. Hanson, L. H. Willems van Beveren, B. Witkamp, L. M. K. Vandersypen, and L. P. Kouwenhoven, Single-shot read-out of an individual electron spin in a quantum dot, *Nature* **430**, 431 (2004).
  - [12] G. Burkard, T. D. Ladd, A. Pan, J. M. Nichol, and J. R. Petta, Semiconductor spin qubits, *Rev. Mod. Phys.* **95**, 025003 (2023).
  - [13] J. Eastoe, G. M. Noah, D. Dutta, A. Rossi, J. D. Fletcher, and A. Gomez-Saiz, Method for efficient large-scale cryogenic characterization of CMOS technologies, *IEEE Transactions on Instrumentation and Measurement* (2024).
  - [14] B. Patra, R. M. Incandela, J. P. Van Dijk, H. A. Homulle, L. Song, M. Shahmohammadi, R. B. Staszewski, A. Vladimirescu, M. Babaie, F. Sebastiano, *et al.*, Cryo-CMOS circuits and systems for quantum computing applications, *IEEE Journal of Solid-State Circuits* **53**, 309 (2017).

- [15] S. Sze and K. Ng, *Physics of Semiconductor Devices*, 3rd ed. (Wiley, 2007).
- [16] K. Matocha, Challenges in SiC power MOSFET design, *Solid-State Electronics* **52**, 1631 (2008), papers Selected from the International Semiconductor Device Research Symposium 2007 – ISDRS 2007.
- [17] H. Chen, P. M. Gammon, V. A. Shah, C. Fisher, C. W. Chan, S. Jahdi, D. Hamilton, M. R. Jennings, M. Myronov, D. R. Leadley, and P. A. Mawby, Cryogenic characterization of commercial SiC power MOSFETs, in *Silicon Carbide and Related Materials 2014*, Materials Science Forum, Vol. 821 (Trans Tech Publications Ltd, 2015) pp. 777–780.
- [18] H. Gui, R. Ren, Z. Zhang, R. Chen, J. Niu, F. Wang, L. M. Tolbert, B. J. Blalock, D. J. Costinett, and B. B. Choi, Characterization of 1.2 kV SiC power MOSFETs at cryogenic temperatures, in *2018 IEEE Energy Conversion Congress and Exposition (ECCE)* (IEEE, 2018) pp. 7010–7015.
- [19] A. Beckers, F. Jazaeri, and C. Enz, Theoretical limit of low temperature subthreshold swing in field-effect transistors, *IEEE Electron Device Letters* **41**, 276 (2019).
- [20] H. Yoshioka, J. Senzaki, A. Shimozato, Y. Tanaka, and H. Okumura, N-channel field-effect mobility inversely proportional to the interface state density at the conduction band edges of SiO<sub>2</sub>/4H-SiC interfaces, *AIP Advances* **5**, 017109 (2015).
- [21] D. Neamen, *Semiconductor Physics and Devices*, 4th ed. (McGraw-Hill, 2012).
- [22] A. J. Lelis, R. Green, D. B. Habersat, and M. El, Basic mechanisms of threshold-voltage instability and implications for reliability testing of SiC MOSFETs, *IEEE Transactions on Electron Devices* **62**, 316 (2014).
- [23] A. J. Lelis, R. Green, and D. B. Habersat, SiC MOSFET threshold-stability issues, *Materials Science in Semiconductor Processing* **78**, 32 (2018), wide band gap semiconductors technology for next generation of energy efficient power electronics.
- [24] S. J. Angus, A. J. Ferguson, A. S. Dzurak, and R. G. Clark, Gate-defined quantum dots in intrinsic silicon, *Nano Letters* **7**, 2051 (2007).

## Appendix: Extended datasets

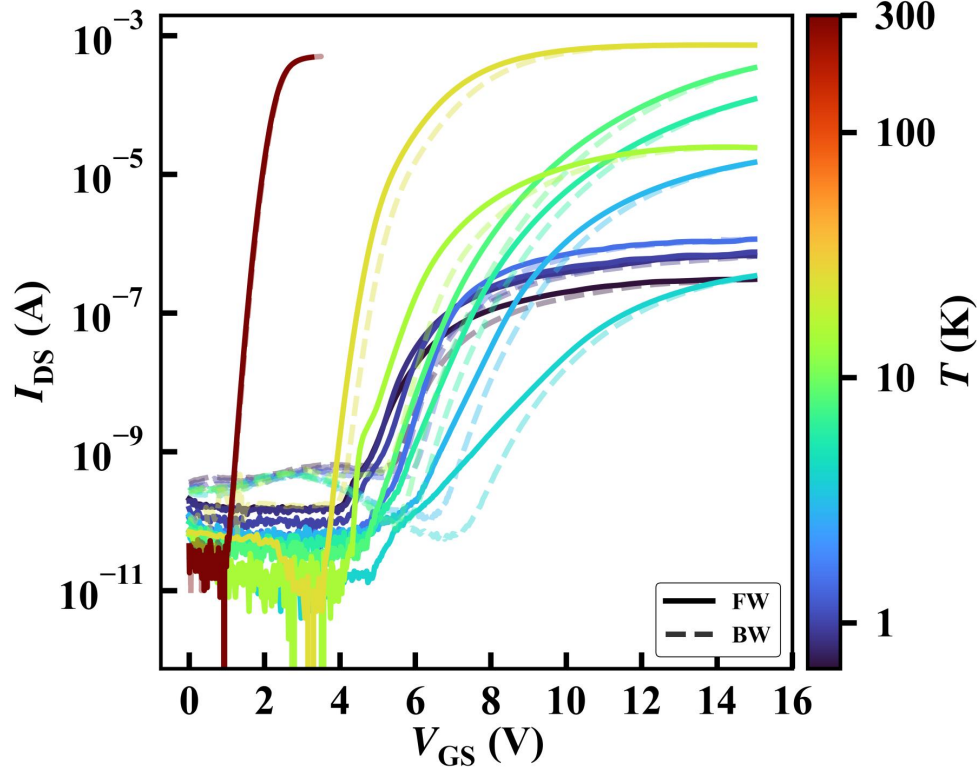


FIG. 5.  $I_{\text{DS}}-V_{\text{GS}}$  transfer characteristics for Device A as a function of temperature measured with forward (solid lines) and backward (dashed lines) gate sweeps.  $V_{\text{DS}}^{0.65 \text{ K}} = 3.8 \text{ V}$ ,  $V_{\text{DS}}^{0.85 \text{ K}} = 3.5 \text{ V}$ ,  $V_{\text{DS}}^{1 \text{ K}} = 3.2 \text{ V}$ ,  $V_{\text{DS}}^{1.5 \text{ K}} = 2.7 \text{ V}$ ,  $V_{\text{DS}}^{3 \text{ K}} = 2.4 \text{ V}$ ,  $V_{\text{DS}}^{4 \text{ K}} = 2.1 \text{ V}$ ,  $V_{\text{DS}}^{6 \text{ K}} = 2.4 \text{ V}$ ,  $V_{\text{DS}}^{8 \text{ K}} = 2.4 \text{ V}$ ,  $V_{\text{DS}}^{15 \text{ K}} = 2.0 \text{ V}$ ,  $V_{\text{DS}}^{25 \text{ K}} = 1.7 \text{ V}$ , and  $V_{\text{DS}}^{300 \text{ K}} = 0.05 \text{ V}$ .

$T$ (K)	$V_0$ (V)	$d$ (nm)
0.65	1.07	23.67
0.85	0.98	19.32
1.5	1.64	13.46
4	1.41	10.00
6	1.24	8.83
15	0.66	8.75

TABLE I. The parameter results of fitting Device A's output characteristics to the Fowler-Nordheim tunneling model shown in Equation 2.



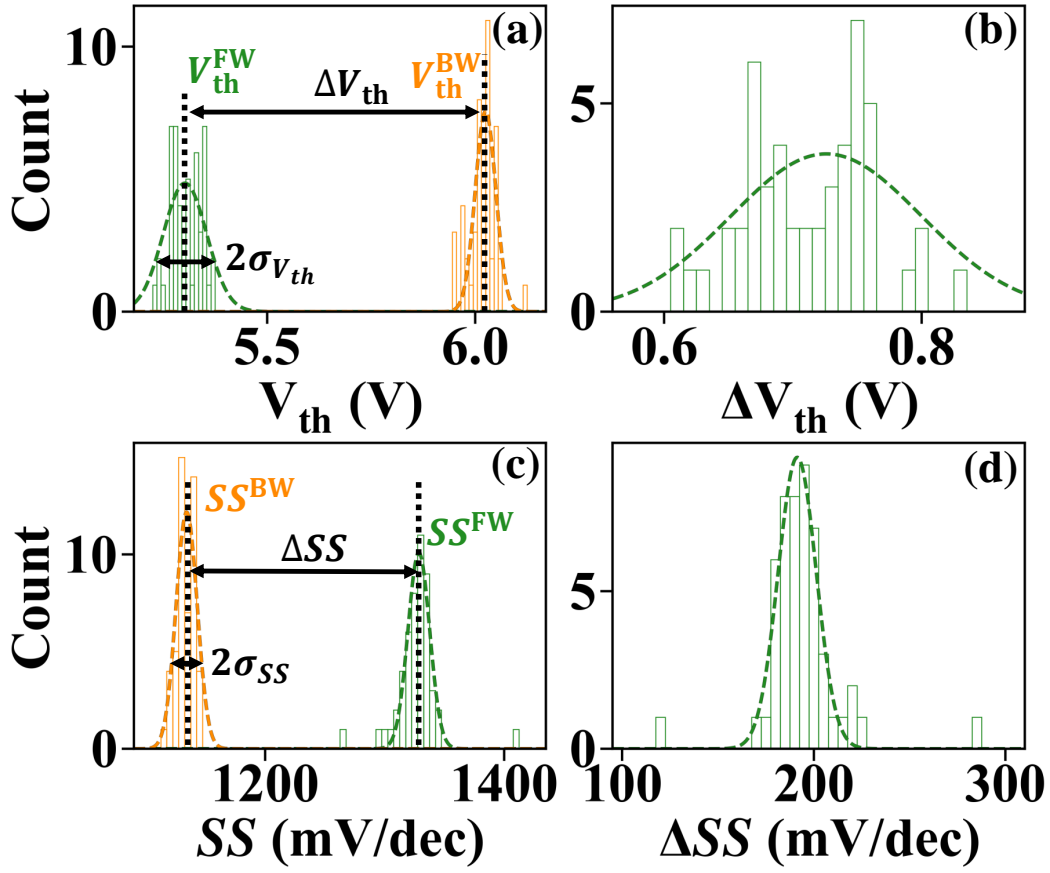


FIG. 6. Device A's statistical distributions at  $T = 0.65$  K used to extract (a)  $V_{th}$  and  $\sigma_{V_{th}}$ , (b)  $\Delta V_{th}$ , (c)  $SS$  and  $\sigma_{SS}$ , (d)  $\Delta SS$ .

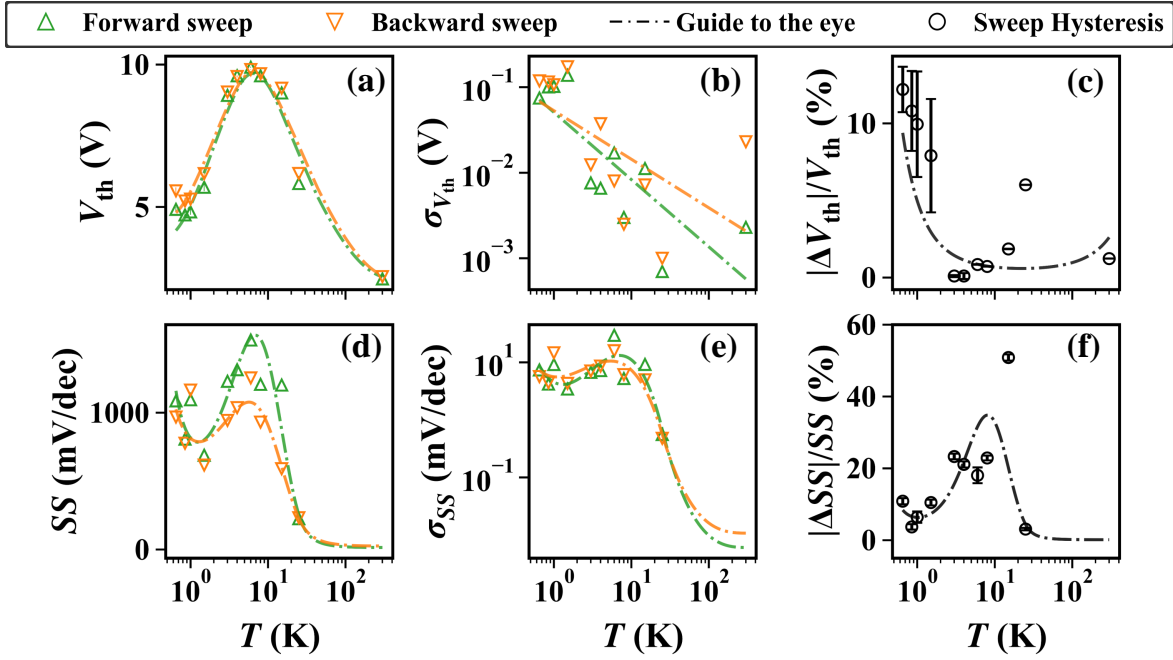


FIG. 7. Parameters extracted from statistical distributions of 50 characteristics as functions of temperature for Device B. The dot-dashed lines in each panel represent guides to the eye to aid evaluation of temperature dependencies. The error bars in (c) and (f) indicate a  $\pm 1\sigma$  spread of the relevant distribution.